AIAA JOURNAL
Vol. 45, No. 1, January 2007

Thrust Measurements from a Finite-Span Flapping Wing

K. Parker* and J. Soria†
Monash University, Melbourne, Victoria 3168, Australia
and
K. D. von Ellenrieder‡
Florida Atlantic University, Dania Beach, Florida 33004-3023

DOI: 10.2514/1.18217

The thrust per unit length behind a flapping NACA0030 airfoil with an aspect ratio of three is measured and presented. Aspects of the evolution of vorticity behind the thrust-producing wing are discussed based on quantitative experiments. Multiple planes of stereoscopic particle image velocimetry measurements are conducted at several locations along the span of the wing at a Strouhal number of 0.35. Of particular interest is the effect of wingtip vortices on the structure of the flow behind the oscillating wing. Wing kinematics is responsible for the flow structure in the 2-D airfoil case. Here, the spanwise distribution of vorticity is found to be dominated, in the large scale, by a single pair of intense counter-rotating vortices. Each member of the large-scale vortex pair is constituted by two smaller corotating vortices that constructively merge in the initial stages of flow separation. Toward the wingtips, three-dimensional effects are more significant. The spatiotemporal variations of transverse and spanwise vorticity in these regions suggest severe local flow deformation. Measurements reveal that flow morphology is highly complex and three-dimensional, unlike any previously observed 2-D wing-based vortex sheets. Furthermore, using 2-D particle image velocimetry data, a sinusoidal variation in thrust force, 90 deg out of phase with the airfoil motion, is measured in the midspan region of the airfoil. The largest measured thrust occurs at the maximum angles of attack, corresponding to the creation of strong leading-edge vortices.

Nomenclature

AR	=	wing aspect ratio, b/c
b	=	wing span from tip to tip, mm
c	=	airfoil chord length from leading edge to trailing edge, mm
f	=	oscillation frequency, Hz
$h(t)$	=	lateral/heave oscillation amplitude as a function of time, mm
h_0	=	maximum amplitude of heave oscillation, mm
k	=	dimensionless reduced frequency, $2\pi fc/U_\infty$
Re_c	=	dimensionless Reynolds number, $U_\infty c/\nu$
St	=	dimensionless Strouhal number, fc/U_∞
U, V, W	=	mean velocity components in the x, y, and z directions, respectively; mm · s^{-1}
u, v, w	=	instantaneous velocity components in the x, y, and z directions, respectively; mm · s^{-1}
x, y, z	=	rectangular Cartesian coordinates in physical space, mm
t	=	time, s
Δt	=	time interval separating each image pair, s
$\theta(t)$	=	pitch angular oscillation amplitude as a function of time, deg
θ_0	=	maximum amplitude of angular oscillation, deg
μ	=	dynamic viscosity, kg · m^{-1}s^{-1}
ν	=	kinematic viscosity, μ/ρ
ρ	=	fluid density, kg · m^{-3}
ψ	=	phase angle between heave and pitch oscillations, deg
ω	=	vorticity in vector notation, s^{-1}
$\omega_x, \omega_y, \omega_z$	=	instantaneous vorticity in x, y, and z directions; s^{-1}
$\langle\rangle$	=	denotes ensemble or phase-averaged quantity

Received 15 June 2005; accepted for publication 15 August 2006.

*Post Doctoral Fellow, Clayton Campus, Department of Mechanical Engineering, Laboratory for Turbulence Research in Aerospace and Combustion; currently Professor, Department of Mechanical Engineering, Cape Peninsula University of Technology, P.O. Box 1906, Bellville 7535, South Africa. Member AIAA.

†Professor, Clayton Campus, Department of Mechanical Engineering, Laboratory for Turbulence Research in Aerospace and Combustion. Fellow AIAA.

‡Professor, Department of Ocean Engineering. Senior Member AIAA.

I. Introduction

MANY aspects of unsteady wings have been extensively studied [1]. Flapping-wing propulsion is one such aspect that has generated and received considerable attention recently [2]. Flapping is defined as a complex combination of heaving and pitching oscillations. Flapping-wing propulsion is a technology that has developed from biomimetic engineering, which is the use of natural science in engineering applications [3]. The perceived optimal efficiency of bird and insect flight has provided scientists with the initial desire to mimic these motions [4]. However, the study of flapping wings is not limited to propulsion alone and can provide valuable insight into other phenomena.

Aeroelastic flutter, which is the result of coupling between the structural dynamics of a wing with the aerodynamics of the flow around it, is still a major concern for the modern aircraft industry [5]. The onset of flutter highlights how vortex shedding can induce undesirable vibrations, with potentially catastrophic failure. On the other hand, flapping wings can be used to study dynamic stall [6] and active flow control [7]. These phenomena have desirable effects that focus primarily on the ability to dynamically control and redistribute vorticity in the flow. This can be accomplished either through some artificial mechanism introduced into the flow, such as external excitation or pulsing jets [8], or by the presence of other downstream flapping wings such as in a tandem arrangement [3,9]. All these phenomena can be broadly categorized as unsteady oscillatory flows.

Although flapping wings have been extensively studied, the focus has been on the flow over nominally 2-D airfoils, for which wingtip effects are negligible. Flow visualizations were used to describe the unique vortical patterns associated with the different parameters that describe the flow condition [10,11]. Using these 2-D airfoil experiments, the oscillation amplitude and frequency play an important role in the characteristics of the vortex street for a

thrust-producing flapping wing [2]. Subsequently, pressure and force measurements then focused on determining the levels of thrust that can be obtained [12,13]. Concurrently, numerical methods were investigating power extraction and propulsion in flapping wings using two-dimensional unsteady panel methods [2] and other inviscid numerical techniques [14]. Notwithstanding, quantitative measurements were conducted using LDV [3] and particle image velocimetry (PIV) [15,16] and provided valuable insight into aspects of the evolution of spanwise vorticity in a reverse Kármán vortex street. Generally, past studies have found that thrust can be optimally produced when the wing operates in combinations of parameters. The dimensionless Strouhal number, which is similar to the reduced frequency used in some studies [17], was found to be the principal wake parameter. St is defined as

$$St = \frac{fA}{U_\infty} \tag{1}$$

where A represents the maximum excursion of the wing trailing edge (double amplitude of oscillation, equals c) and U_∞ represents the freestream velocity. In the range $\{0.25 \leq St \leq 0.4\}$, thrust is optimally produced. Anderson [13,16] found that for high-efficiency and high-thrust conditions, the reverse Kármán vortex street is ubiquitous. Furthermore, Koochesfahani [11] found that sinusoidal flapping oscillations produce the clearest reverse Kármán vortex street in the wake pattern. In this case, two vortices per cycle are the optimal pattern. Any other oscillation profile created added vortices that degraded the generation of trust and propulsive performance.

Comparatively, much less experimental and numerical data have been generated for finite-span wings. Cheng and Murillo [18] were amongst the first to assert that the effect of wing three dimensionality cannot be neglected in any measurement of thrust efficiency or formulation of a numerical method. Also, the effect of tip vortices becomes more significant at lower aspect ratios. Qualitative dye-flow experiments by Parker et al. [19,20] show that the wingtips significantly modify the structure of the wake flow. This results in a variation from the conventional reverse Kármán vortex street. However, parametric visualization experiments suggest that finite-span wings are affected in a similar way to infinite-span wings, by the parameters that govern the wing kinematics [19–21]. Therefore, it is appropriate to apply the same airfoil kinematics for optimal thrust production in 2-D airfoils, to 3-D airfoils.

Based on further qualitative experiments, von Ellenrieder et al. [22] proposed a 3-D vortex skeleton of the flow behind a 3-D flapping wing [22], shown in Fig. 1. It can be seen that the flow structure is highly contorted and forms interconnected loops from alternating leading- and trailing-edge vortices. Note that the material lines (representing vorticity) originate from the wing surface and do not just end in the flow. The filaments on the right-hand side of Fig. 1 would connect to a similar structure from the previous oscillation cycle. The illustration is a snapshot of a periodic structure. Further details pertaining to Fig. 1 are discussed by von Ellenrieder et al.

However, interpretations of highly unsteady flows from dye visualizations can be circumstantial due to misinterpretation of the actual flow [23]. Consequently, quantitative PIV measurements were performed in the plane of symmetry of a finite-span flapping wing. Measurements verify the existence of pairs of counter-rotating vortices that populate the flow [24,25]. Using a triple decomposition approach similar to Hussain [26], the measurements along the centerline reveal that large coherent structures form when the flow separates from the oscillating wing, forming a reverse Kármán vortex street. Nonetheless, the apparent complex and three-dimensional nature of the flow in these preliminary experiments highlights the need for more comprehensive spanwise measurements in the area surrounding the wingtips. Spatially varying measurements are required to elucidate the model proposed in Fig. 1.

Recently, numerical studies by Guglielmini and Blondeaux [27] have corroborated some aspects of the proposed flow structure in Fig. 1, at $St = 0.35$. Guglielmini and Blondeaux suggest, from numerical investigations, that the leading-edge vortices are much stronger than the trailing-edge vortices when the wing oscillates by a distance greater than or equal to the wing chord. Furthermore, a Kármán vortex streetlike structure results when leading- and trailing-edge vortices join [28]. Although there have been other useful quantitative studies, their focus is primarily related to animal locomotion. In this study, the aim is to understand how the morphological characteristics of this complex flow can influence the motion of the wing.

There has been considerably more progress in the development of numerical methods to predict thrust production, and to a lesser degree, the flow characteristics on finite-span wings. Jones et al. [29,30] and Tuncer and Platzer [31] used both Navier–Stokes solvers and inviscid potential flow models to predict the effect of various motion parameters on the thrust characteristics of a NACA0012 airfoil. The separate effects of a parameter referred to in literature as "reduced frequency" (similar to the Strouhal number) and oscillation amplitude were studied and found to be of primary importance to thrust producibility. More recent computations by Guglielmini and Blondeaux [27], Blondeaux et al. [32], and Dong et al. [33] investigated the wake structure and performance of finite aspect-ratio flapping foils. Once again, models of the flow structure presented from these studies closely resemble the model previously proposed in Fig. 1.

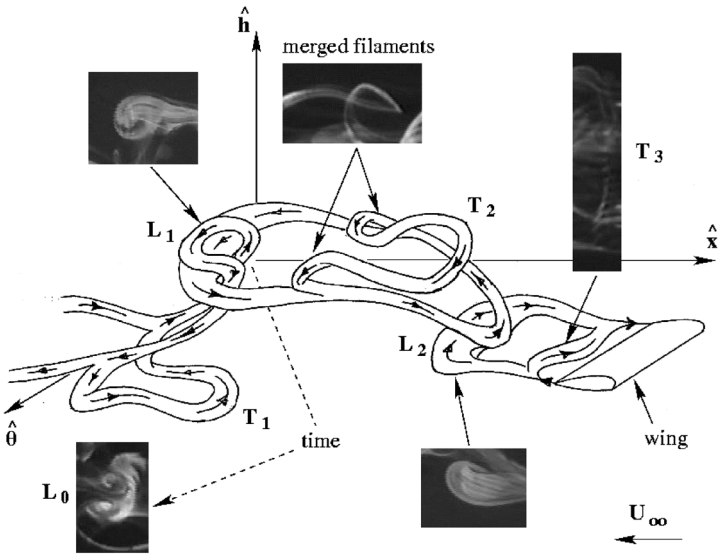

Fig. 1 Proposed three-dimensional vortex skeleton behind a finite aspect-ratio flapping wing [22].

In an unsteady three-dimensional flow such as this, the evolution of vorticity is very important in characterizing the flow structure. Preliminary experiments indicate that airfoil kinematics, thrust production, and flow morphology are all related. Of interest here is to investigate the nature of this interaction. This is inherently a tedious exercise and can also be inefficiently applied. Using multiple planes of stereoscopic multigrid cross-correlation digital particle image velocimetry (SMDPIV), the three components of velocity can be resolved in three dimensions. This permits the resolution of all vorticity components at several regions along the span of the wing. The initial section of the results in this paper discusses the flow morphology in the context of three-dimensional vorticity evolution. The measurement methodology employed here permits accurate and repeatable multipoint measurements of the flow in a spatiotemporal sense. The total thrust force imparted by the oscillating airfoil to the fluid can be calculated using a net momentum approach, using the mean velocity profiles from the PIV data.

The present set of experiments permits the use of the momentum integral equation to calculate the mean centerline thrust per unit length at each oscillation phase using the phase-averaged velocity profiles. The latter part of the results relates the measured thrust to the wing kinematics as well as to the flow morphology.

II. Experimental Technique

The experiments are conducted in the 5-m recirculating horizontal water tunnel at the Laboratory for Turbulence Research in Aerospace and Combustion. The properties of the test section and the specific details of the apparatus, data acquisition, and measurement analysis are provided in Parker et al. [25]. Some information of the experimental methodology is presented here. A NACA0030-type wing is suspended vertically above the test section, as shown in Fig. 2. The airfoil oscillates about the quarter-chord point. The heave and pitch oscillations are stepper motor driven and described by Eqs. (2) and (3) for heave and pitch motions, respectively. The two oscillations are related by a phase angle.

$$h(t) = h_0 \cos(2\pi f t) \tag{2}$$

$$\theta(t) = \theta_0 \cos(2\pi f t + \psi) \tag{3}$$

where $h_0 = c/2$ and heave frequency equals pitch frequency. The stepper motors are computer-controlled. Figure 2 shows the experimental setup and illustrates some of the primary components in the apparatus. An angular-offset stereo configuration with a camera angle of 64_deg is used to acquire the stereo PIV images. As shown in Fig. 2, three Pixelfly CCD cameras, with array sizes of 1280×1024 px each, are mounted vertically onto a three-axis translation stage, below the test section. Each camera is fitted with a 55-mm Micro Nikkor Nikon lens. Once the experiment has been fine-tuned and prepared, the camera acquisition and laser light sheet optics are constrained and only the wing is allowed to move in the z direction for different spanwise measurements. Some novel modifications to the experimental methodology allowed for improved measurements in the liquid flow environment. This arrangement and procedure ensured repeatability of the experiments with minimal interference [25].

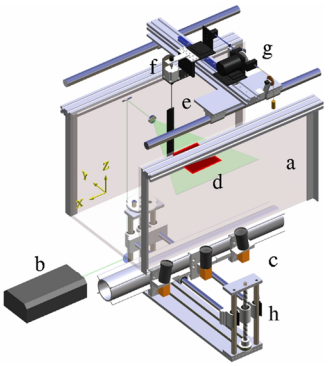

Fig. 2 Schematic of the experimental apparatus. Labels correspond to a, test section; b, laser; c, stereo-CCD camera arrangement; d, horizontal light sheet with central measurement region highlighted; e, wing mounted on vertical translation stage; f, pitch stepper motor; g, heave stepper motor with scotch yoke; and h, three-axis translation stage.

Eight phase-averaged SMDPIV measurements are conducted in a region 4 c (y direction) by 3 c (x direction). Each phase average is calculated from 500 single-exposed instantaneously acquired PIV images separated by dt. The random error in the velocity measurements is 1%, at the 99% confidence level. Images of the flow are acquired in three planes spaced a distance equivalent to the PIV measurement grid spacing. The vorticity and other derived quantities are calculated by applying a center difference approach across the three closely spaced x–y planes. The sets of PIV images are analyzed using a multigrid cross-correlation scheme by Soria [34]. The two-dimensional, two-component vector fields are combined to form a three-dimensional, two-component vector field using a stereo reconstruction algorithm, developed in-house by StereoMagik. An in situ calibration technique, similar to that used by Solof et al. [35], is used here. The calibration data are used with a vector-valued mapping function to calculate the three components of displacement in the object plane. The selected mapping function has a cubic dependence on the in-plane velocity component and a quadratic dependence on the out-of-plane component to allow it to adequately track any distortions in the stereo measurements. The largest error in the measured displacement is 0.0001 mm in the measurement field of 80×40 mm. The procedure for validating the SMDPIV experiments is extensively discussed in [25].

III. Experimental Results

The results of the SMDPIV experiments are presented for $Re = 637$, $\psi = 90$ deg, $\theta_0 = 5$ deg, and $St = 0.35$. This test condition corresponds to an optimal thrust-producing case for a 2-D airfoil (no wingtips), as described by Anderson [13]. Phase-averaged vorticity is calculated in the x, y, and z directions using the velocity gradients from the multiple plane measurements. The measurement planes are differentially spaced by Δz, as shown in Fig. 3. A local least-squares approach similar to that used by Soria and Fouras [36] is used to calculate the vorticity. From 400 instantaneous velocity fields, the vorticity is calculated at eight phases in the motion trajectory of the airfoil described in Table 1. In all cases, the vorticity is phase-locked with the motion of the wing.

In all cases, the phase-averaged vorticity $\langle\omega_x\rangle$, $\langle\omega_y\rangle$, and $\langle\omega_z\rangle$ measurements at the midspan and 1/4 c from the wingtip and wingtip regions are shown superimposed onto the $\langle uv\rangle$ surface streamline patterns. These z regions are designated by R_0, R_1, and R_2, respectively, and are illustrated in Fig. 3. A typical flow visualization image from von Ellenrieder et al. [22] of the wing at phase 1 is shown in Fig. 3. Note that in this case, the flow direction is reversed (left to right). From the planform view of the flow visualization, the midspan region R_0 experiences much greater vortical interactions and is a

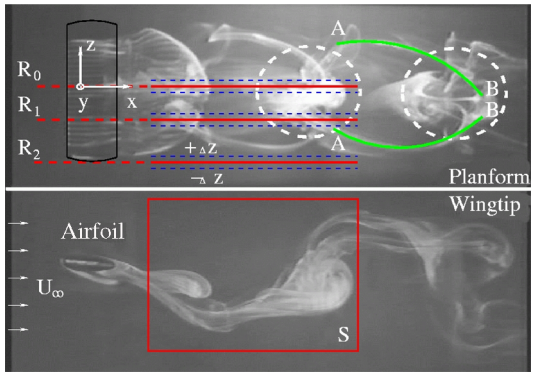

Fig. 3 A typical flow visualization image behind a flapping wing with an aspect ratio of three at $St = 0.35$.

Table 1 Phase information for which PIV data are acquired

label	Phase	$h(t)$	$\theta(t)$
a	1	$-h_0$	0
b	2	$-0.707h_0$	$+\theta_0/2$
c	3	0	$+\theta_0$
d	4	$+0.707h_0$	$+\theta_0/2$
e	5	$+h_0$	0
f	6	$+0.707h_0$	$-\theta_0/2$
g	7	0	$-\theta_0$
h	8	$-0.707h_0$	$-\theta_0/2$

region of immense activity. Therefore, a measurement in this plane is expected to capture the physical characteristics that will allow comparison with the vortex model by [22], presented in Fig. 1. Closer to the wingtips, the measurements will capture the filaments of the vortex structures, shown in Fig. 3.

The SMDPIV measurements correspond to region S in Fig. 3. This region is offset by 1/4 c from the trailing edge of the wing. This is due to an obstruction of the wing in the line of sight of the right stereo camera. The convection velocity U_∞ has been removed from the stream traces, whereas the vorticity is nondimensionalized by a heave oscillatory timescale $\dot{h}_{\max}/A$, where $\dot{h}_{\max} = 31.46$ mm $\cdot$ s^{-1} and $A = c = 20$ mm. Flow is from left to right. The wing $c/4$ location is selected as the origin. Because the period of oscillation of the wing is 2 s, any vorticity created at the wing surface will be seen roughly 1 s later within the measurement domain. In this time, the wing would have moved to another phase location 1 s later. As a result, any interpretation of the measurements with respect to the wing location must consider this mismatch.

Figure 4 illustrates the orientation of each calculated vorticity component in relation to the Cartesian reference frame applied to the measurements. In Fig. 3, the red area is clearly marked by the label S in the x–y plane (wingtip view). The same area is marked as a red straight line in the planform view. This region S is the red area marked in Fig. 4 and indicates the measured area. The green areas in Fig. 4 are the three Cartesian reference planes, as indicated by the axis labels. The direction of the freestream velocity is clearly marked in each . Because measurements were conducted in horizontal planes, shown as region S, the $\langle\omega_x\rangle$ and $\langle\omega_y\rangle$ vorticity is effectively applicable only to each 4-mm z region.

IV. Discussion

A. Velocity Profiles

The properties of the mean flow velocity components are calculated for each z region. In Figs. 5a–5c, the mean velocity profiles of the x, y, and z components of velocity are shown across the y direction for each measured z region.

Each velocity is acquired at $x/c = 3.0$, nondimensionalized by the mean centerline velocity U_c, and calculated from all phase data, namely, 3200 vector fields. The mean heave profiles are symmetrical about the mean heave axis $h = 0$ for the three regions. Only half of the total profile is shown in Fig. 5. For Fig. 5 only, $h = 0$ corresponds to $y/c = 0$ and $h = +10$ mm corresponds to $y/c = 1.5$. The airfoil heave oscillation is between $y/c = -1.5$ and $y/c = +1.5$, corresponding to $h = -h_0$ and $h = +h_0$, respectively.

From the U velocity component in Fig. 5a, it can be seen that the profile resembles a jet for region R_0, with U_c 25% greater than the mean flow velocity away from the core. In region R_1, the situation is

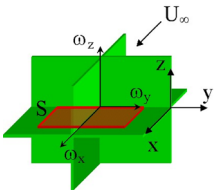

Fig. 4 Schematic illustrating the definition of resolved vorticity in the context of the measurement area S.

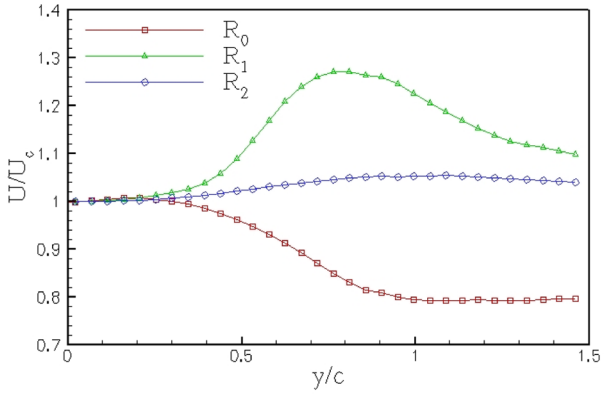

a)

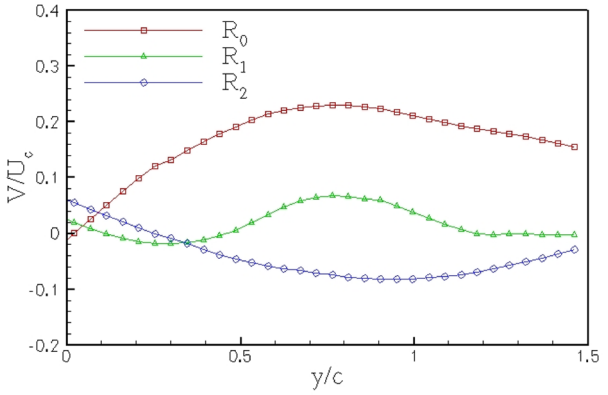

b)

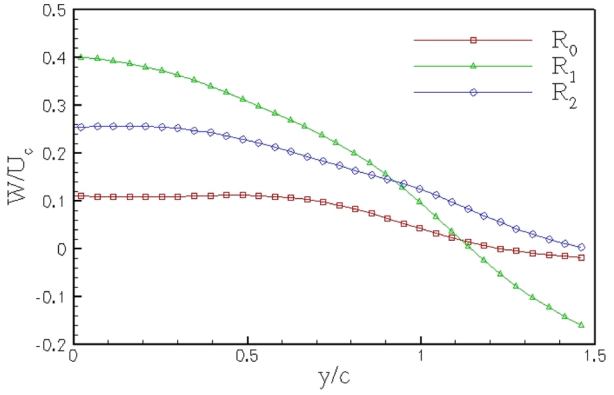

c)

Fig. 5 Mean velocity profiles at $x/c = 3.0$ measured in each region for components a) U, b) V, and c) W; $h = 0$ corresponds to $y/c = 0$ and $h = +10$ mm corresponds to $y/c = 1.5$. Every second measurement is shown.

inverted, with centerline velocity less than 25% of the mean flow velocity at $y/c = 0.75$. This value is further reduced from the core region, to 10% at $y/c = 1.5$. The mean streamwise velocity exhibits the least variation from U_c for region R_2, which is 2 mm from the wingtip. This suggests that the flow in this region is equivalent to the mean freestream value. From Fig. 5b, all regions show that the transverse velocity component is significantly smaller than the centerline velocity in the freestream direction.

The behavior of the V velocity component for each region is inverted, compared with the U velocity component. In Fig. 5c, the mean W velocity profiles resemble a jet in all regions. At $x/c = 3.0$, the largest mean out-of-plane velocity of 0.4 U_c is measured in the central z region R_1. In the region around $y/c = 1.45$ away from the jet core, the flow appears to be largely dominated by U and W for R_1 and R_2 with $V < 0.05\,U_c$. For R_0, the magnitude of V is more significant. The magnitude of the centerline velocity relative to U, V,

and W suggests that the flow in the core region is dominated by the streamwise component, followed by the spanwise component.

B. Phase-Averaged Vorticity

Based on preliminary 2-D PIV measurements by Parker et al. [25], it was expected that spanwise vorticity would dominate the flow evolution, rather than the streamwise and transverse vorticity components. However, this experiment has proved this to be incorrect for some z regions as well as phases.

At each of the wing locations shown in Figs. 20–22, the wing is orientated at either of the extreme heave or pitch positions. This results in the formation of a region of separated flow from the wing surface and the creation of spanwise vorticity at the leading edge (at $+\theta_0$ and $+\theta_0$) or trailing edge (at $+h_0$ and $-h_0$). The tabular format in which the data are presented is meant to provide a sense of the spatial and temporal variation of vorticity. In all the isocontour plots presented, positive counterclockwise (CCW) vorticity is off of the page.

The vorticity magnitude $|\omega|_{\max}$ is 0.169 s^{-1}, 0.150 s^{-1}, and 0.052 s^{-1} in regions R_0, R_1, and R_2, respectively. In region R_1, $\langle\omega_x\rangle$ dominates the vorticity magnitude by up to 0.5 $|\omega|_{\max}$. In the case of $\langle\omega_y\rangle$ and $\langle\omega_z\rangle$, the magnitude is more evenly distributed in each z region. In general, the spatial distribution of spanwise vorticity in a plane from R_0 to R_2 lies closer to the trailing edge for planes closer to the wingtips. This can be seen in Fig. 22 (label c), in which vorticity of the same sign is measured at lower x/c as planes move closer to the wingtips. When streamlines of the in-plane velocity are superimposed onto the spanwise vorticity contours in Fig. 22, it can be seen that foci in each plane corresponding to a particular region of strong $\langle\omega_z\rangle$ lie along a diagonal. Overall, the spatial location of spanwise vorticity in Fig. 22 suggests that the measurement plane is intersecting a vortex tube, possibly tilted in the z axis. This is similar to filament AB, highlighted in green in Fig. 3. Figure 6 illustrates this physical characteristic of the flow structure. It shows a cross-sectional view of the structure in each x–y plane, but with all z planes linking the structure together, thus forming a conical tubelike member.

Over one flapping cycle, low levels of $\langle\omega_x\rangle$ compared with $|\omega|_{\max}$, corresponding to pairs of corotating streamwise vorticity, are measured along region R_0. Vorticity $+\langle\omega_z\rangle$ is first measured in R_0 at $\phi 1$ in two separate spatial locations. At this phase, the airfoil has reached an extreme heave oscillation location, $-h_0$. In the second half of the oscillation, the airfoil reaches $+h_0$ at $\phi 5$ and introduces $-\langle\omega_z\rangle$ into measurement area S. The tilting effect is also observed for $\langle\omega_x\rangle$, particularly in Fig. 20 (label c). This suggests that the vortical structure may be tilted in the x axis also. In region R_1, the flow is characterized by a pair of $-\langle\omega_x\rangle$ at $\phi 1$, but only one region of $+\langle\omega_x\rangle$ is measured at $\phi 5$ in Fig. 20 (label f). The measured dominance of $\langle\omega_x\rangle$ over $\langle\omega_y\rangle$ and $\langle\omega_z\rangle$ in R_0 is not apparent at the wingtips in R_2. Here, the flow is characterized by a single concentration of $-\langle\omega_x\rangle$ at $\phi 1$ and $+\langle\omega_x\rangle$ at $\phi 5$. When comparing the introduction of streamwise vorticity to the motion of the airfoil, it is clear that at $\phi 3$ (Fig. 20, label c) and $\phi 7$ (not shown), when the airfoil reaches the extreme pitch angles of attack, no significant changes in the vorticity magnitude occur.

In general, the flowfield is characterized by two pairs of oppositely signed transverse vorticity component $\langle\omega_y\rangle$ in each flapping cycle.

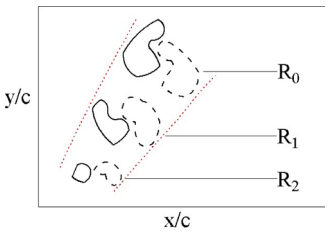

Fig. 6 Illustration of the tilting nature of the structures observed in each z region.

Each vortex pair is constituted of $+\langle\omega_y\rangle$ and $-\langle\omega_y\rangle$ closely lumped together. This first appears when the airfoil reaches $-h_0$ and $+h_0$ at $\phi 1$ and $\phi 5$, respectively. The spatial extent of $+\langle\omega_y\rangle$ is up to 2.5 times the spatial size of regions of $\langle\omega_z\rangle$ in region R_0. The peak magnitude of $+\langle\omega_y\rangle$ and $-\langle\omega_y\rangle$ is $0.3|\omega|_{\max}$. On the other hand, no noticeable change in the phase-averaged vorticity occurs when the airfoil reaches $+\theta_0$ or $-\theta_0$. As observed for $\langle\omega_x\rangle$ and $\langle\omega_z\rangle$, the x–y location of regions of intense $\langle\omega_y\rangle$ are tilted in z regions approaching the wingtips. In R_1, the counter-rotating pairs of $\langle\omega_y\rangle$ are spatially smaller. At some phases, such as in Fig. 21 (labels c and e), the regions of $-\langle\omega_y\rangle$ are larger than $+\langle\omega_y\rangle$. This is opposite to the case for region R_0. A threshold of 30% of $|\omega|_{\max}$ is applied to the isocontour plots for all regions. The magnitude of ω_y is greatly reduced and barely visible at the wingtip region in Fig. 21. In region R_2, the wingtip vortices are expected to dominate the flow dynamics. Unlike R_0 and R_1, the vorticity does not convect completely to the end of the measurement area over a cycle. At $\phi 1$ and $\phi 5$, vorticity is barely visible. The vorticity that appears at other phases disappears intermittently from the measurement plane.

Figure 22 shows that the evolution of $\langle\omega_z\rangle$ is characterized by a single pair of large-scale counter-rotating vorticity about $h = 0$ ($y/c = 1.5$). The large-scale structures in region R_0 form a reverse Kármán vortex streetlike pattern similar to the 2-D PIV case previously observed [25]. On closer scrutiny, Fig. 22 reveals that each large-scale structure reveals two smaller corotating regions of $\langle\omega_z\rangle$ that lump together in a consolidated manner. The direction of roll-up of the streamlines is clockwise (CW) for $-\langle\omega_z\rangle$ at $\phi 1$, whereas in Fig. 22, the streamlines roll up CCW for the $+\langle\omega_z\rangle$ first introduced in the measurement area. Although the results reveal discernible regions of intense spanwise vorticity in all z regions, the peak $\langle\omega_z\rangle$ in R_0 accounts for $0.2|\omega|_{\max}$, which is less than the peak $\langle\omega_x\rangle$.

When compared with the maximum heave oscillation frequency, the peak spanwise vorticity is $\mathcal{O}(6\dot{h}_0/c)$. In contrast, the peak $\langle\omega_z\rangle$ in R_1 and R_2 is up to $0.3|\omega|_{\max}$. Measurements for each phase at each z region show more compact regions of vorticity of similar rotation in regions closer to the wingtip. This suggests that, as before, each measurement plane intersects a conically shaped vortex tube or roll-up with the largest circumference at the midspan region. The introduction of $\langle uv\rangle$ streamlines superimposed onto the vorticity contours in Fig. 22 reveals that not all regions of intense $\langle\omega_z\rangle$ convect at U_∞. In cases such as in Fig. 22 (label a), at $\phi 1$–R_0, the region of high $+\langle\omega_z\rangle$ at $x/c = 3$ is ahead of the focus in the streamline pattern. In contrast, no significant change in the flow occurs when the airfoil reaches θ_0 at $\phi 3$ or $\phi 7$.

On the other hand, at $\phi 4$–R_0, the region of high $+\langle\omega_z\rangle$ at $x/c = 5$) is behind the focus. This repeated observation suggests that as a consequence of the wake growing and structures convecting, there is significant mutual and self-induction affecting the rotation of vorticity. In these cases, $+\langle\omega_z\rangle$ at $\phi 4$ and $-\langle\omega_z\rangle$ at $\phi 1$ enter the measurement area S as two smaller regions lumped together as a single larger region. In subsequent phases, these corotating regions appear to separate and convect into opposite directions of y/c. At the wingtip, relatively high levels of vorticity are measured, yet the streamlines exhibit no unique foci. Instead, the foci appear to converge along a line in the downstream direction, forming a seam in the flowfield.

V. Thrust Production in Flapping Wings

The general form of the momentum theorem for a control volume V bounded by a control surface S states that the force vector on the fluid inside the control volume is equal to the material derivative of the fluid momentum integrated over the volume [37]:

$$\boldsymbol{F} = \frac{\mathrm{D}}{\mathrm{D}t}\int_V \rho\bar{v}\,\mathrm{d}V = \int_V \frac{\partial}{\partial t}(\rho\bar{v})\,\mathrm{d}V + \int_S \rho\overline{vv}\cdot\hat{\boldsymbol{n}}\,\mathrm{d}S \qquad (4)$$

where $\hat{\boldsymbol{n}}$ is the local normal vector along the control surface. The first term of the momentum equation is the rate of change of momentum

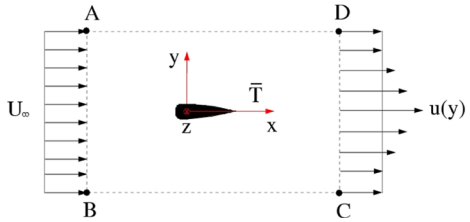

Fig. 7 Control volume for momentum analysis.

inside the control volume, whereas the second term accounts for the momentum flux across the control volume boundary. The force vector $\boldsymbol{F}$ encompasses all the forces on the control volume, including body forces such as gravity, pressure, and viscous forces on the surface boundaries.

Consider the control volume ABCD around the airfoil in Fig. 7. The boundaries AD and BC are sufficiently far away from the airfoil in the undisturbed fluid that there is negligible momentum flux through these surfaces. At the upstream boundary AB, the velocity across the boundary is the freestream velocity U_∞. At the downstream boundary CD, the velocity across the boundary is $u(y)$. There is no momentum flux across the airfoil surface boundary. If it is assumed that the average flow is steady and incompressible and that the pressure is constant along the control volume boundaries (that is, the downstream pressure is equalized to the freestream value), the thrust on the airfoil can be written in terms of the change in momentum in the x direction. Applying mass conservation, the momentum integral equation becomes [13],

$$T = -F_x = \rho \int_{-\infty}^{+\infty} u(y)[u(y) - U_\infty]\,\mathrm{d}y \tag{5}$$

which is exactly the same result obtained by von Kármán for the drag on a flat plate in terms of the momentum defect. The simplified momentum integral is one of the few methods [13] able to provide

Table 2 Table of thrust ratio for each phase ϕ

ϕ	h, mm	θ, deg	T_r
1	$-h_0$	0	0.98
2	$-0.7h_0$	$+0.7\theta_0$	0.38
3	0	$+\theta_0$	0.8
4	$+0.7h_0$	$+0.7\theta_0$	1.6
5	$+h_0$	0	0.96
6	$+0.7h_0$	$-0.7\theta_0$	0.39
7	0	$-\theta_0$	1.21
8	$-0.7h_0$	$-0.7\theta_0$	1.56

an indication of the variation in the mean centerline thrust per unit span.

The momentum integral used to calculate thrust in Sec. VI accounts for the variation in the axial velocity as a function of the transverse position y only. To verify that the wake had been adequately captured in the y direction, the difference in the upstream and downstream velocity is calculated and is shown in Fig. 8 as a function of y/c. The velocity difference $\Delta U = [u(y) - U_\infty]$ is represented as a ratio of the centerline difference $\Delta U_c = (U_c - U_\infty)$, which represents the maximum velocity addition to the mean flow. It can be seen that the end of the profile tends to zero at the point at which the jet velocity has reached freestream.

$$T_r = \langle T_\phi \rangle / \bar{T} \tag{6}$$

Equation (5) is applied to each of the eight phase-averaged velocity measurements yielding $\langle T_\phi \rangle$. In Eq. (6), the thrust ratio is defined as the ratio of $\langle T_\phi \rangle$ to the mean thrust from all phases $\bar{T}$. The corresponding values are listed in Table 2.

The thrust ratio exhibits a sinusoidal variation about the mean thrust value. The peak thrust levels are 60% greater than the mean thrust, with maximum at $\phi = 4$ and 8 and minimum at $\phi = 2$ and 6. The mean thrust measured is 0.0032 N. This corresponds to the

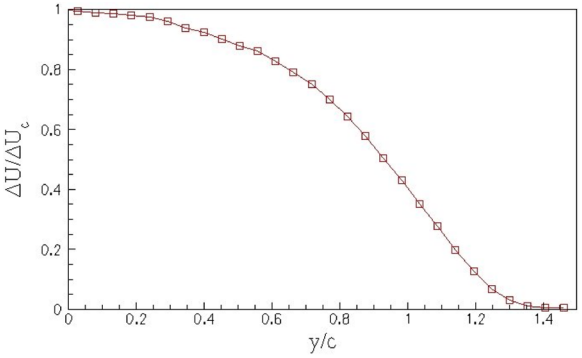

Fig. 8 Plot of mean velocity addition across jet half-width at $x/c = 3$. Every third measurement is shown.

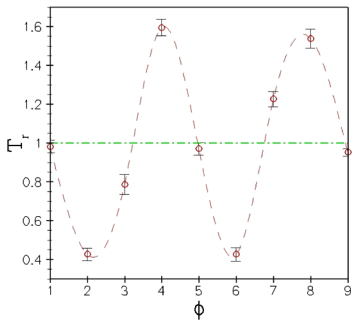

Fig. 9 Mean thrust ratio in Eq. (6), measured at various phases along the trajectory of a finite-span flapping airfoil.

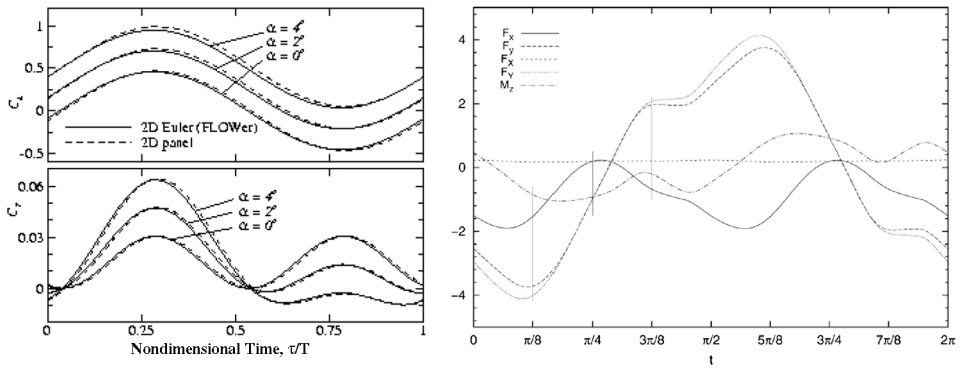

Fig. 10 Mean thrust measurement behind a flapping airfoil, extracted from past studies: a) courtesy of Jones et al. [29] and b) courtesy of Guglielmini et al. [27].

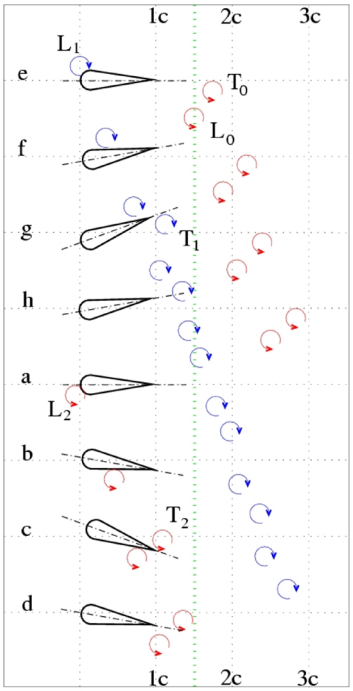

Fig. 11 Evolution of vorticity behind a 3-D flapping wing at $St = 0.35$. The definition of each label (a–h) is presented in Table 1.

airfoil phase location when the data are acquired. Table 2 lists the measured thrust ratios in relation to the heave and pitch orientation of the airfoil. When the airfoil reaches each of the extreme heave locations, $(-h_0, +h_0)$, the thrust at that phase equals the mean centerline thrust. When the airfoil moves toward the maximum angles of attack, the thrust corresponds to either the largest or smallest value, compared with the mean centerline thrust per unit span.

The distribution of the mean centerline thrust ratio from Eq. (6) is shown in Fig. 9 at each of the airfoil phase locations ϕ. Figure 9 indicates that peak thrust is measured at $h_0/2$ and $\theta_0/2$. Because h_0 and θ_0 are the peak oscillation amplitudes, the results suggest that the production of centerline thrust is 90 deg out of phase with the airfoil heave motion. When the airfoil is at h_0 and θ_0, the phase-averaged $\langle T_\phi \rangle$ is equal to the mean thrust per unit length.

In absolute force units, the thrust can be estimated from the airfoil motion in the freestream and heave directions, U_∞ and $\dot{h}_0$, respectively. Using the span area of the airfoil $S = b \times c$ and the lift equation $F = C_f \frac{1}{2} \rho u^2 S$, an estimate of the force in the freestream direction can be obtained. If C_f is assumed to be one, an upper estimate of the total thrust force is obtained. In this case, a value of 0.0011 N is obtained, compared with the measured mean thrust per unit length of 0.0032 $\mathrm{N \cdot m^{-1}}$.

As mention in the Introduction, phase-related thrust measurements for finite-span airfoils were not found in the literature at the time of going to press. Data are more readily available for two-dimensional airfoils but wingtip losses are neglected. To provide some simple comparisons, two more relevant thrust curves were selected from past studies. Figure 10a shows the forces predicted by several inviscid numerical schemes by Jones et al. [2] on an infinite-span airfoil at reduced frequency $k = 0.2$, $St = 0.03$ for various mean angles of attack α, and $Re_c = 10^6$. A 2-D Euler solver and 3-D panel code are used to predict the flow physics. The upper graph is the lift coefficient C_L and the lower graph is the thrust coefficient C_T. Figure 10b shows the thrust force on an infinite-span airfoil as predicted by Guglielmini and Blondeaux [27] using a numerical solution of the vorticity equation. Absolute force in newtons is shown for half of the airfoil cycle. Several curves representing the various force and moments in the flowfield are

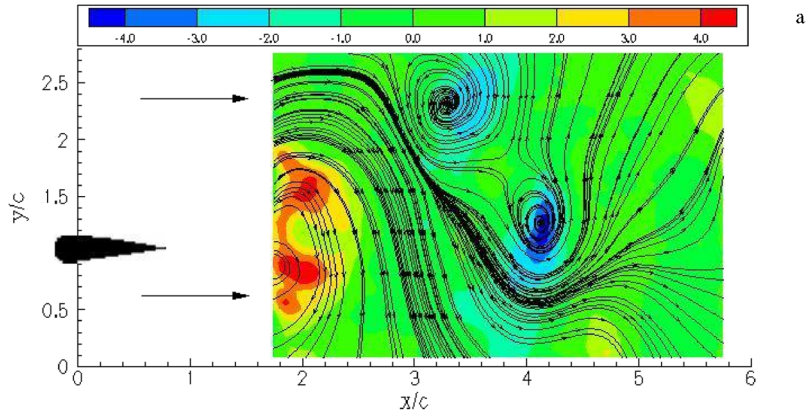

Fig. 12 Spanwise vorticity $\langle \omega_z \rangle / |\omega|_{\max}$ in region R_0 at $\phi 1$. The isocontours are superimposed onto the in-plane velocity streamlines $\langle u \rangle$ and $\langle v \rangle$.

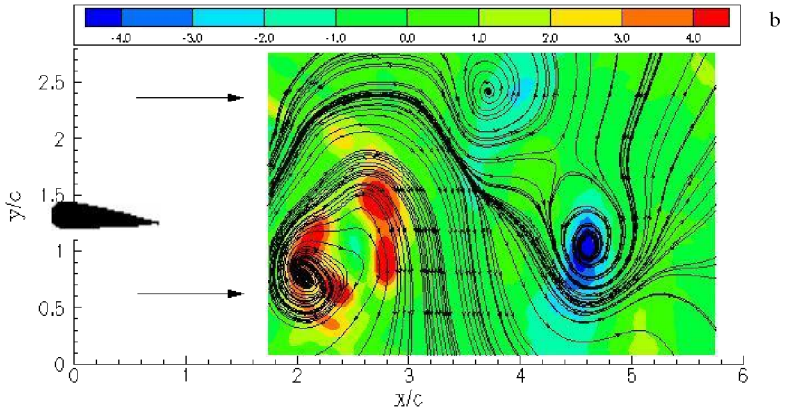

Fig. 13 Spanwise vorticity $\langle \omega_z \rangle / |\omega|_{\max}$ in region R_0 at $\phi 2$. The isocontours are superimposed onto the in-plane velocity streamlines $\langle u \rangle$ and $\langle v \rangle$.

shown. Parameter $-F_x$ represents the thrust force in the x direction. The problem is that such two-dimensional methods of calculation overestimate thrust production, because they take into account only the energy from cross-stream wake vorticity normal to the motion and omit trailing vorticity in the streamwise direction.

Nonetheless, the two inviscid numerical solvers employed by Jones et al. [2] predict similar results. Similarly, the results of Guglielmini and Blondeaux [27] also indicate a sinusoidal-like thrust profile. Although the experimentally calculated thrust ratio in Fig. 9 also shows a sinusoidal variation with airfoil phase angle, locations of peak thrust do not correspond. Direct comparison between past and present measurements is not possible, because the experimentally measured thrust is the mean centerline value per unit length, whereas the absolute values by Jones et al. and Guglielmini et al. were calculated from the predicted instantaneous pressure distribution around the airfoil.

The thrust variation appears to peak at $\{\pi/4, 3\pi/2\}$ and $\{\pi/4, 3\pi/4\}$ for the predicted values, respectively, whereas the measured values peak at $3\pi/4$ and $7\pi/4$ in Fig. 9. From the apparent lack of consensus, it is clear that the restrictive nature of the measured thrust has not satisfied the need for more precise measurement of the thrust produced by the airfoil. Nonetheless, the present measurements indicate that a similar mean velocity based method can be used to calculate the mean thrust. Furthermore, the results here suggest that the mean thrust is phase-locked with the motion of the airfoil and not constant. Contrary to expectation, the temporal variation of the

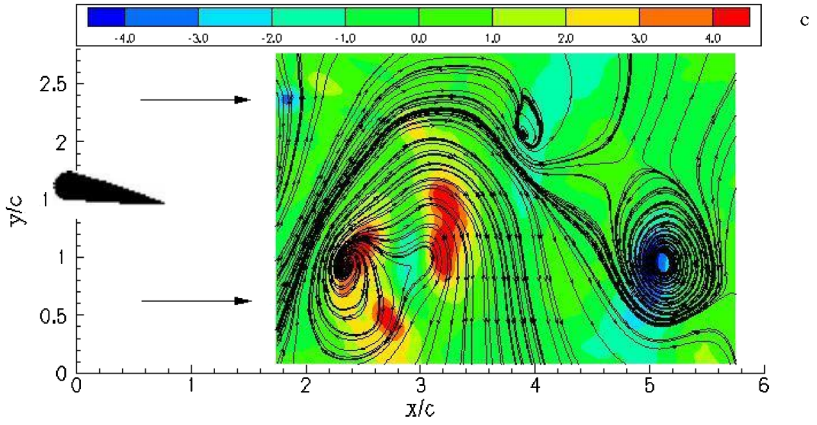

Fig. 14 Spanwise vorticity $\langle\omega_z\rangle/|\omega|_{\max}$ in region R_0 at $\phi 3$. The isocontours are superimposed onto the in-plane velocity streamlines $\langle u\rangle$ and $\langle v\rangle$.

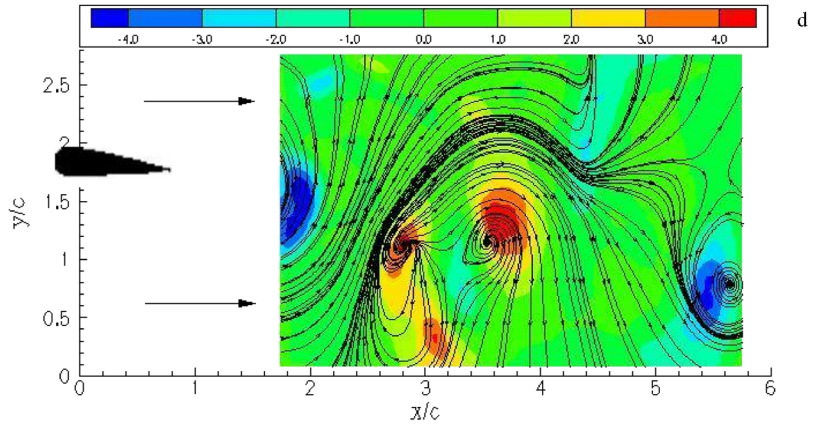

Fig. 15 Spanwise vorticity $\langle\omega_z\rangle/|\omega|_{\max}$ in region R_0 at $\phi 4$. The isocontours are superimposed onto the in-plane velocity streamlines $\langle u\rangle$ and $\langle v\rangle$.

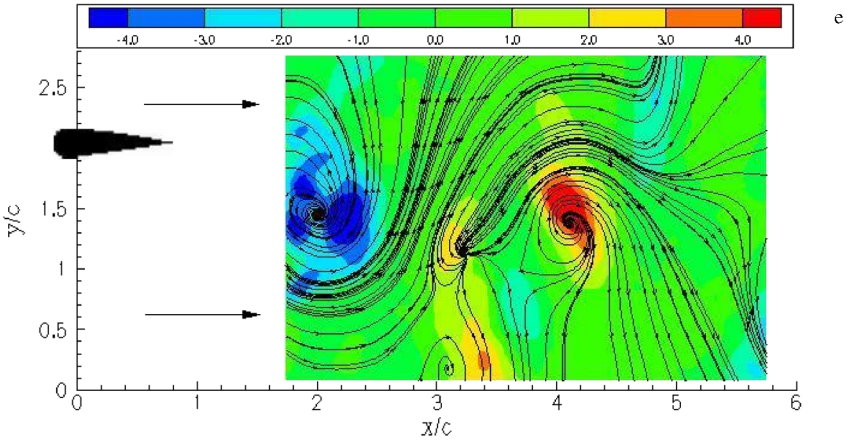

Fig. 16 Spanwise vorticity $\langle\omega_z\rangle/|\omega|_{\max}$ in region R_0 at $\phi 5$. The isocontours are superimposed onto the in-plane velocity streamlines $\langle u\rangle$ and $\langle v\rangle$.

measured thrust per unit length does not follow the phase that dominates the morphological variations of the flow.

The thrust estimate determined here is associated with the reverse Kármán vortex street in the plane of symmetry of the airfoil. Koochesfahani [11] found that the creation of a reverse Kármán vortex street is associated with minimal energy and therefore optimal thrust efficiency. The measured vortex street is a combination of leading- and trailing-edge vortices. The formation of a strong leading-edge vortex in flapping airfoils is normally associated with the phenomenon of dynamic stall. When this occurs, the airfoil experiences a sudden but unsustainable increase in lift.

By analyzing the evolution of vorticity along the centerline of the flapping wing, the vortex street can be tracked and the spanwise orientations can be traced. A detailed discussion of this is provided by Parker et al. [38]. Using this method, Fig. 11 is developed and represents a map of the vortices as they evolve and convect. In this section, this map is compared to the previously mentioned thrust distribution in Fig. 9.

The evolution of spanwise vorticity over one oscillation sequence is presented in Figs. 12–19. At $\phi 4$ (label d) and $\phi 8$ (label h), T_r reaches maximum levels, which is expected to correspond to the phase averages snapshot of intense counterclockwise and clockwise vorticity shed from the airfoil and observed in measurement region S. This is in agreement with Fig. 11.

Because of the location of the measurement area in relation to the wing, as well as the known oscillation period, the observed flow

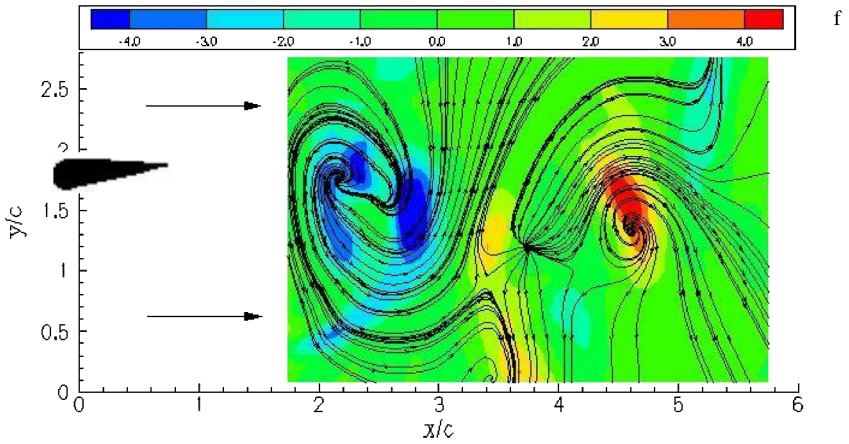

Fig. 17 Spanwise vorticity $\langle\omega_z\rangle/|\omega|_{max}$ in region R_0 at $\phi 6$. The isocontours are superimposed onto the in-plane velocity streamlines $\langle u\rangle$ and $\langle v\rangle$.

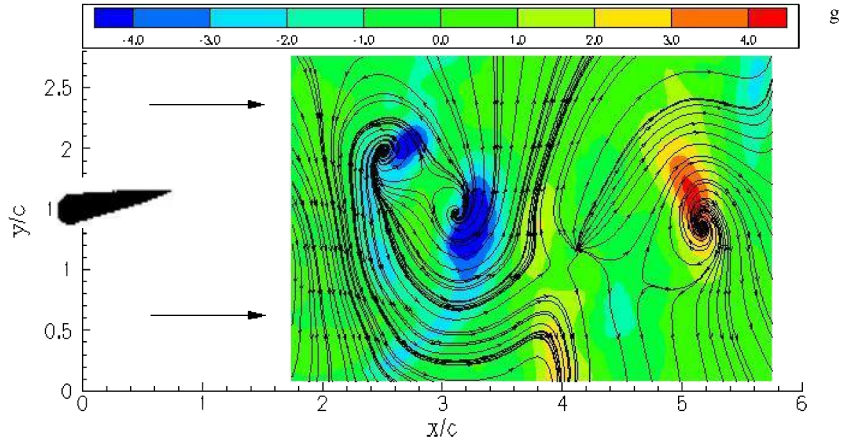

Fig. 18 Spanwise vorticity $\langle\omega_z\rangle/|\omega|_{max}$ in region R_0 at $\phi 7$. The isocontours are superimposed onto the in-plane velocity streamlines $\langle u\rangle$ and $\langle v\rangle$.

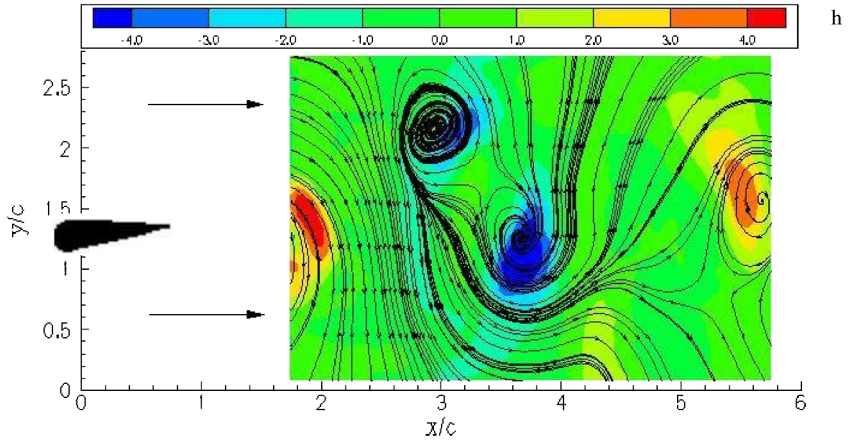

Fig. 19 Spanwise vorticity $\langle\omega_z\rangle/|\omega|_{max}$ in region R_0 at $\phi 8$. The isocontours are superimposed onto the in-plane velocity streamlines $\langle u\rangle$ and $\langle v\rangle$.

snapshots (from Figs. 15 and 19, for example) represent the actual flow interaction at the wing, 1 s prior to measurement. This corresponds to $\phi 2$ (label b) and $\phi 6$ (label f) in Fig. 11. This measurement is associated with a leading-edge vortex appearing on the suction side of the airfoil.

Similarly, at $\phi 2$ (label b) and $\phi 6$ (label f), T_r reaches minimum levels, which is expected to correspond to the presence of a CCW and CW leading-edge vortex on the airfoil suction side in Fig. 11 and CCW and CW vorticity in measurement region S. The latter pair of vortices are observed in the measurement region S in Figs. 13 and 17, respectively. As before, the event resulting in the vortices in Figs. 13 and 17 would have occurred 1 s earlier. This corresponds to $\phi 8$ (label h) and $\phi 4$ (label d) in Fig. 11. These phases immediately precede the formation of a leading-edge vortex.

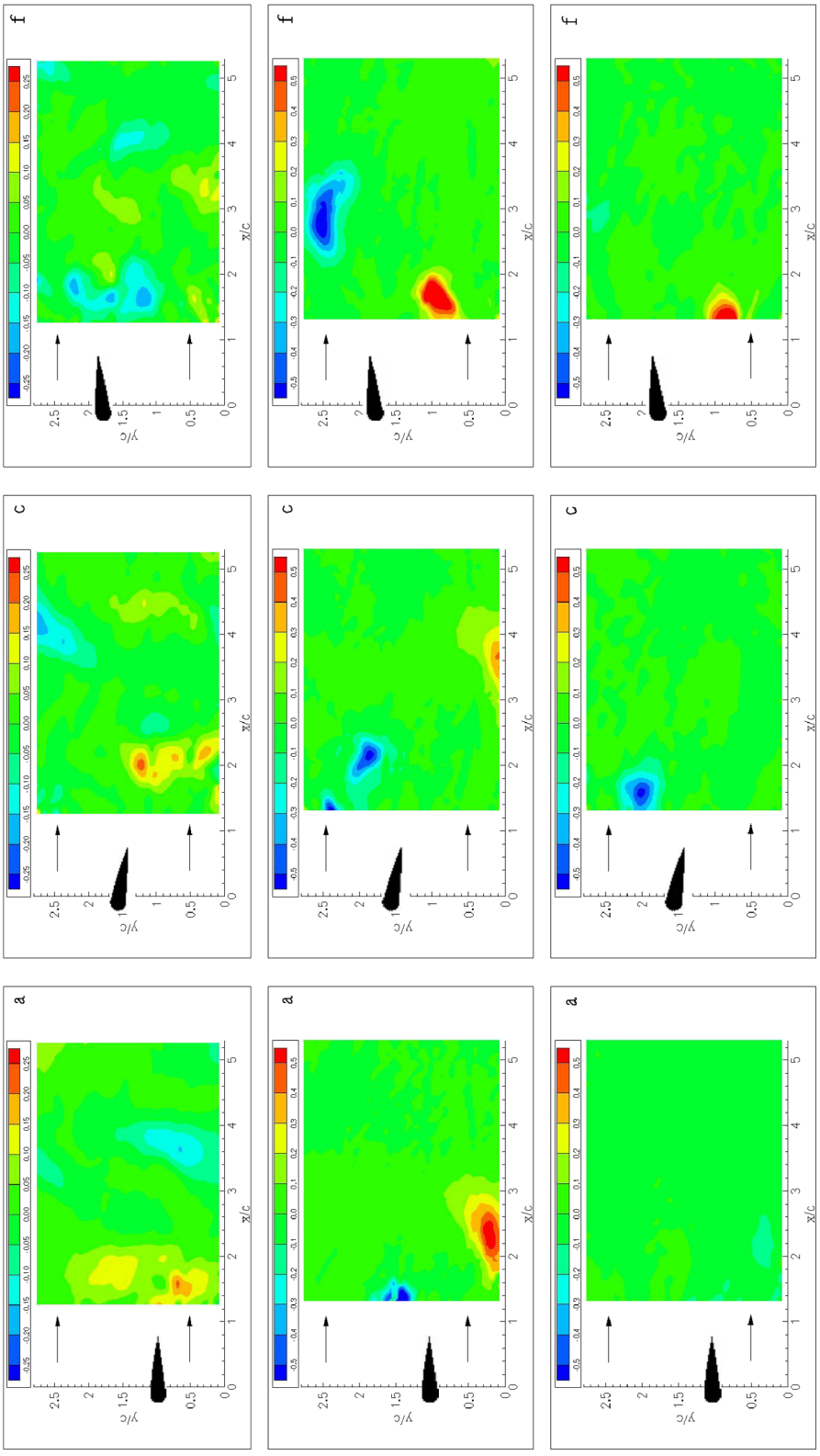

Fig. 20 Spatiotemporal distribution of the streamwise component of vorticity $\langle \omega_x \rangle / |\omega|_{\max}$. Rows 1, 2, and 3 represent regions R_0, R_1, and R_2, respectively. Each column corresponds to phases $\phi 1$, $\phi 3$, and $\phi 6$.

VI. Conclusions

Based on the results of this study, in the plane of symmetry of a finite-span wing, the three-dimensional effects due to wingtip vortices are negligible compared with leading and trailing vortices. After each half cycle, leading- and trailing-edge vorticity of similar rotation is shed into the flow. During the initial stages of vortex shedding, this vorticity merges to form large-scale structures. This process is repeated in the next half-cycle, except with opposite vorticity. Thus, after each half cycle, the flow is populated by a coherent, counter-rotating vortex pair. Transverse vorticity dominates the flow in this location, drawing fluid away from the

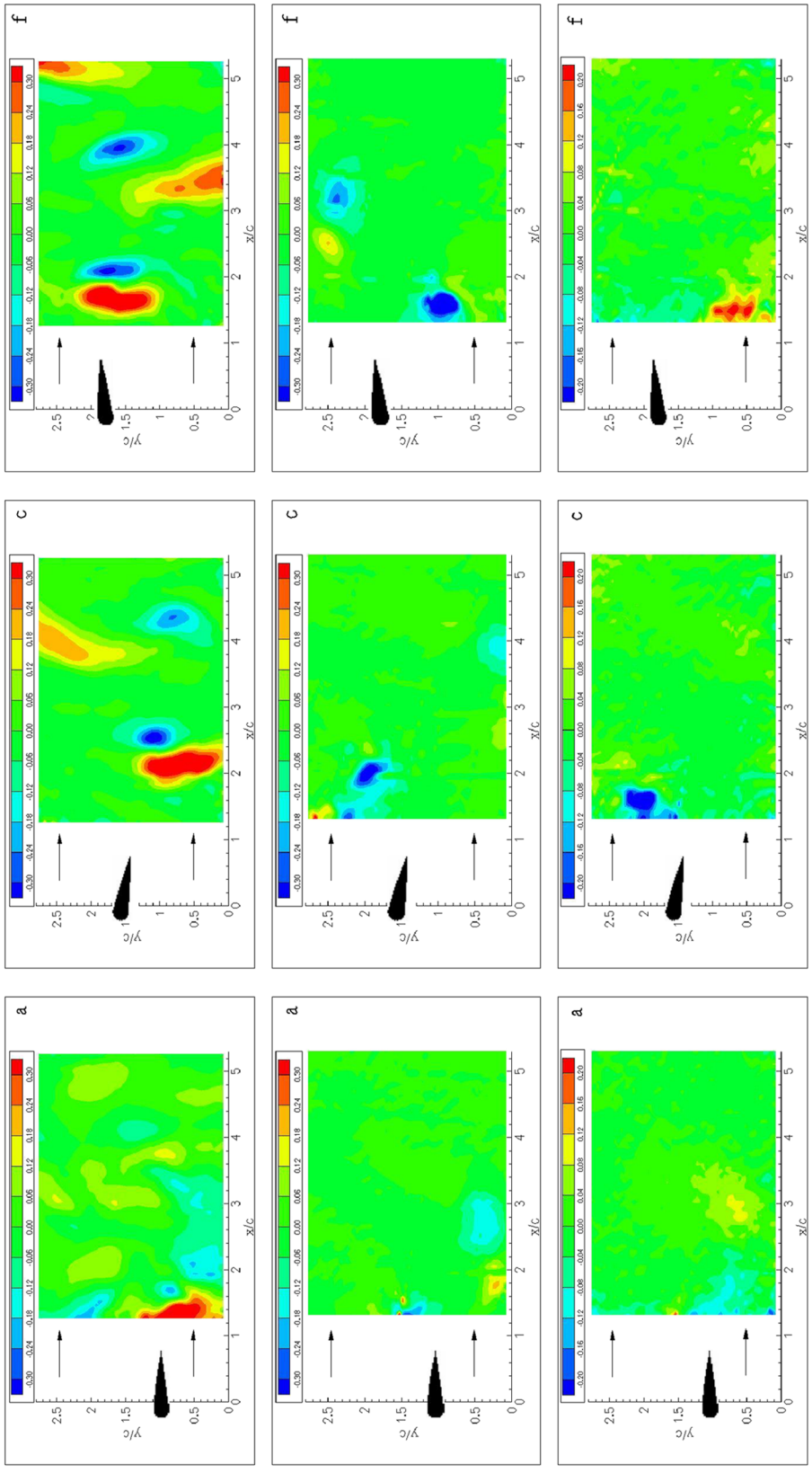

Fig. 21 Spatiotemporal distribution of the transverse component of vorticity $\langle\omega_y\rangle/|\omega|_{\max}$. Rows 1, 2, and 3 represent regions R_0, R_1, and R_2, respectively. Each column corresponds to phases $\phi 1$, $\phi 3$, and $\phi 6$.

wingtips into the direction of oscillation of the wing as well as the mean flow.

Closer to the ends, the wingtip vortices dominate and the leading- and trailing-edge vortices become less intense and distinguishable. Only single streamers of intense vorticity are observed. Spanwise vorticity and streamwise vorticity dominate the flow and follow the motion of the wing. In general, the measurements reveal a highly complex flow structure that exhibits all the characteristics associated with local amplification, stretching, and tilting of vortex filaments.

The variation in the mean centerline thrust per unit length resembles a sine wave. The location of minimum or maximum thrust values corresponds to the creation of strong leading-edge vortices.

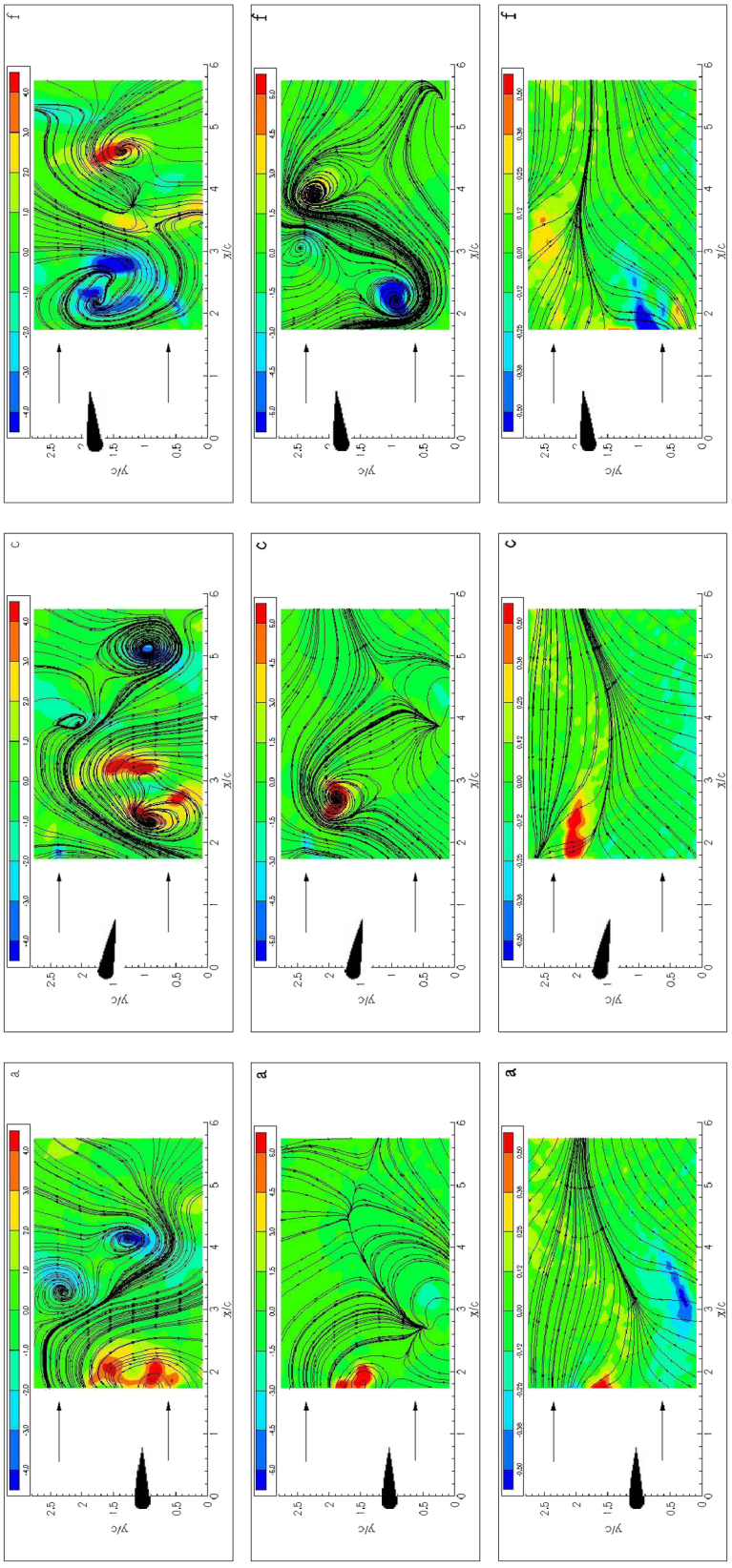

Fig. 22 Spatiotemporal distribution of the spanwise component of vorticity $\langle\omega_z\rangle/|\omega|_{\max}$. Rows 1, 2, and 3 represent regions R_0, R_1, and R_2, respectively. Each column corresponds to phases $\phi 1$, $\phi 3$, and $\phi 6$.

References

[1] McCroskey, W. J., "Unsteady Airfoils," *Journal of Fluid Mechanics*, Vol. 14, 1982, pp. 285–311.

[2] Jones, K. D., Castro, B. M., Mahmoud, O., Pollard, S. J., Platzer, M. F., Neef, M. F., Gonet, K., and Hummel, D., "A Collaborative Numerical and Experimental Investigation of Flapping-Wing Propulsion in Ground Effect," AIAA Paper 2002-0706, 2002.

[3] Jones, K. D., and Platzer, M. F., "An Experimental and Numerical Investigation of Flapping-Wing Propulsion," AIAA Paper 99-0995, 1999.

[4] Ramamurti, R., and Sandberg, W. C., "Computational Study of 3-D Flapping Flows," AIAA Paper 2001-0605, 2001.

[5] Tuncer, I. A., Walz, R., and Platzer, M. F., "A Computational Study of the Dynamic Stall of a Flapping Airfoil," Naval Postgraduate School, Rept. 98-2519, Monterey, CA, 1998.

[6] Leishman, J. G., "Unsteady Aerodynamics of Airfoils Encountering Travelling Gusts and Vortices," *Journal of Aircraft*, Vol. 34, No. 6, 1997, pp. 719–729.

[7] Gopalkrishnan, R., Triantafyllou, M. S., Triantafyllou, G. S., and Barrett, D., "Active Vorticity Control in a Shear Layer Using a Flapping Foil," *Journal of Fluid Mechanics*, Vol. 274, 1994, pp. 1–21.

[8] Greenblatt, D., and Wygnanski, I. J., "The Control of Flow Separation by Periodic Excitation," *Progress in Aerospace Sciences*, Vol. 36, Oct. 2000, pp. 487–545.

[9] Bandyopadhyay, P. R., Castano, J. M., Rice, J. Q., Philips, R. B., Nedderman, W. H., and Macy, H. K., "Low-Speed Maneuvering Hydrodynamics of Fish and Small Underwater Vehicles," *Journal of Fluids Engineering*, Vol. 119, No. 11, 1997, pp. 136–144.

[10] Freymuth, P., "Propulsive Vortical Signature of Plunging and Pitching Airfoils," *AIAA Journal*, Vol. 26, No. 7, July 1988, pp. 88–883.

[11] Koochesfahani, M. M., "Vortical Patterns in the Wake of an Oscillating Airfoil," *AIAA Journal*, Vol. 27, No. 9, 1989, pp. 1200–1205.

[12] DeLaurier, J. D., and Harris, J. M., "Experimental Study of Oscillating-Wing Propulsion," *Journal of Aircraft*,Vol. 19, No. 5, May 1982, pp. 368–373.

[13] Anderson, J. M., "Vortex Control for Efficient Propulsion," Ph.D. Thesis, Massachusetts Inst. of Technology, Cambridge, MA, and Woods Hole Oceanographic Inst., Woods Hole, MA, Feb. 1996.

[14] Katz, J., and Weihz, D., "Behavior of Vortex Wakes from Oscillating Airfoils," *Journal of Aircraft*,Vol. 50, No. 12, 1978, pp. 861–863.

[15] Panda, J., and Zaman, K. B. M. Q., "Experimental Investigation of the Flow Field of an Oscillating Airfoil and Estimation of Lift from Wake Surveys," *Journal of Fluid Mechanics*, Vol. 265, 1994, pp. 65–95.

[16] Anderson, J. M., Streitlien, K., Barrett, D. S., and Triantafyllou, M. S., "Oscillating Foils of High Propulsive Efficiency," *Journal of Fluid Mechanics*, Vol. 360, 1998, pp. 41–72.

[17] Jones, K. D., Dohring, C. M., and Platzer, M. F., "Experimental and Computational Investigation of the Knoller-Betz Effect," *AIAA Journal*, Vol. 36, No. 7, July 1998, pp. 1240–1246.

[18] Cheng, H. K., and Murillo, L. E., "Lunate-Tail Swimming Propulsion of a Curved Lifting Line in Unsteady Flow," *Journal of Fluid Mechanics*, Vol. 143, 1984, pp. 327–350.

[19] Parker, K., von Ellenrieder, K., and Soria, J., "The Effects of Phase Angle on the Vortical Signatures Behind a Flapping Airfoil of Finite Aspect Ratio," *Fourteenth Australasian Fluid Mechanics Conference* [CD ROM], edited by B. Dally, Adelaide Univ., Adelaide, SA, Australia, Dec. 2001.

[20] Parker, K., von Ellenrieder, K., and Soria, J., "Flow Visualization of the Effect of Pitch Amplitude Changes on the Vortical Signatures Behind a Three-Dimensional Flapping Airfoil," *Optical Technology and Image Processing for Fluids and Solids Diagnostics 2002*, edited by G. X. Shen, S. S. Cha, F.-P. Chiang, and C. R. Mercer, Vol. 5058, SPIE—International Society for Optical Engineering, Bellingham, WA, Apr. 2003, pp. 331–343.

[21] Ohmi, K., Coutanceau, M., Loc, T. P., and Duliec, A., "Vortex Formation Around an Oscillating and Translating Airfoil at Large Incidences," *Journal of Fluid Mechanics*, Vol. 211, 1990, pp. 37–60.

[22] Von Ellenrieder, K. D., Parker, K., and Soria, J., "Flow Structures Behind a Heaving and Pitching Finite-Span Wing," *Journal of Fluid Mechanics*, Vol. 490, 2003, pp. 129–138.

[23] Hama, F. R., "Streaklines in a Perturbed Shear Flow," *Physics of Fluids*, Vol. 5, No. 6, June 1962, pp. 644–650.

[24] Parker, K., von Ellenrieder, K., and Soria, J., "Stereoscopic PIV Measurements of the Flow Past a Circular Cylinder at Reynolds Number 15000," *Proceedings of the Fifteenth Australasian Fluid Mechanics Conference* [CD ROM], edited by M. Behnia, W. Lin, and G. D. McBain, Univ. of Sydney, Sydney, NSW, Australia, 2004; also Australasian Fluid Mechanics Conference Paper AFMC00226.

[25] Parker, K., von Ellenrieder, K., and Soria, J., "Using Stereo Multigrid DPIV Measurements to Investigate the Vortical Skeleton Behind a Finite-Span Flapping Wing," *Experiments in Fluids*, Vol. 39, No. 2, 2005, pp. 281–298.

[26] Hussain, A. K. M. F., "Coherent Structures and Turbulence," *Journal of Fluid Mechanics*, Vol. 173, 1986, pp. 303–356.

[27] Guglielmini, L., and Blondeaux, P., "Propulsive Efficiency of Oscillating Foils," *European Journal of Mechanics, B/Fluids*, Vol. 23, No. 2, 2004, pp. 255–278.

[28] Triantafyllou, M. S., Techert, A. H., and Hover, F. S., "Review of Experimental Work in Biomimetics Foils," *IEEE Journal of Oceanic Engineering*, Vol. 29, Feb. 2004, pp. 585–594.

[29] Jones, K. D., Lai, J. C. S., Tuncer, I. A., and Platzer, M. F., "Computational and Experimental Investigation of Flapping Foil Propulsion," *Proceedings of the 1st International Symposium on Aqua Bio-Mechanisms, ISABMEC 2000* [CD ROM], Tokai Univ. Pacific Center, Honolulu, HA, 2000.

[30] Jones, K. D., Castro, B. M., Mahmoud, O., and Platzer, M. F., "A Numerical and Experimental Investigation of Flapping-Wing Propulsion in Ground Effect," AIAA Paper 2002-0866, 2001.

[31] Tuncer, I. A., and Platzer, M. F., "Thrust Generation Due to Airfoil Flapping," *AIAA Journal*, Vol. 34, No. 2, 1996, pp. 324–331.

[32] Blondeaux, P., Fornarelli, F., Guglielmini, L., Triantafyllou, M. S., and Verzicco, R., "Vortex Structures Generated by a Finite-Span Oscillating Foil," AIAA Paper 2005-84, 2005.

[33] Dong, H., Mittal, R., Bozkurrtas, M., and Najjar, F., "Wake Structure and Performance of Finite Aspect-Ratio Flapping Foils," AIAA Paper 2005-81, 2005.

[34] Soria, J., "An Adaptive Cross-Correlation Digital PIV Technique for Unsteady Flow Investigations," *Proceedings of the 1st Australian Conference on Laser Diagnostics in Fluid Mechanics and Combustion*, edited by A. Masri, and D. Honnery, Univ. of Sydney, Sydney, NSW, Australia, 1996, pp. 29–48.

[35] Soloff, S. M., Adrian, R. J., and Liu, Z. C., "Distortion Compensation for Generalized Stereoscopic Particle Image Velocimetry," *Measurement Science and Technology*, Vol. 8, Sept. 1997, pp. 1441–1454.

[36] Soria, J., and Fouras, A., "Accuracy of Out-Of-Plane Vorticity Measurements Using In-Plane Velocity Vector Field Measurements," *Proceedings of the Twelfth Australasian Fluid Mechanics Conference*, edited by J. Soria, Monash Univ., Melbourne, VIC, Australia, Dec. 1995, pp. 4560–4567.

[37] Batchelor, G., *An Introduction to Fluid Dynamics*, Cambridge Univ. Press, Cambridge, England, U.K., 1967.

[38] Parker, K., von Ellenrieder, K., and Soria, J., "An Experimental Investigation of a 3D Flapping-Wing Flow," *Journal of Fluid Mechanics* (submitted for publication).

W. Ng
Associate Editor